Macrophage-Like Cell Density Is Increased in Proliferative Diabetic Retinopathy Characterized by Optical Coherence Tomography Angiography

Janice X. Ong, Peter L. Nesper, Amani A. Fawzi, Jacob M. Wang, and Jeremy A. Lavine

Department of Ophthalmology, Feinberg School of Medicine, Northwestern University, Chicago, Illinois, United States

Correspondence: Jeremy A. Lavine, Department of Ophthalmology, Feinberg School of Medicine, Northwestern University, 240 E. Huron Street, McGaw Pavilion M343, Chicago, IL 60611, USA; jeremy.lavine@northwestern.edu.

JXO and PLN contributed equally to this work.

PURPOSE. To quantitatively characterize macrophage-like cells (MLCs) at the vitreoretinal interface in different severity stages of diabetic retinopathy (DR) using optical coherence tomography angiography (OCTA).

METHODS. The study included 72 eyes of 72 subjects: 18 healthy controls, 22 diabetes mellitus (DM) without DR, 17 nonproliferative DR (NPDR), and 15 proliferative DR (PDR). We obtained repeated (average, 6.5; range, 3–10) macular OCTA scans for each eye. We registered and averaged the 3-μm OCT slab above the vitreoretinal interface to visualize MLCs. Using a semiautomated method, we binarized and quantified MLCs and compared MLC densities among groups. We also evaluated MLC distribution relative to underlying superficial capillary plexus vasculature and quantified MLCs overlying blood vessels within the perivascular 30-μm watershed region and within ischemic zones (defined as >30 μm from the nearest vessel).

RESULTS. MLC density was 2.8- to 3.8-fold higher in PDR compared with all other groups ($P < 0.05$ for all). MLC density in PDR was most increased in perivascular areas (3.3- to 4.2-fold; $P < 0.05$ vs. all) and on blood vessels (3.0- to 4.0-fold; $P < 0.05$ vs. all), and elevated to a lesser extent in ischemic areas (2.3- to 3.4-fold; $P < 0.05$ vs. all). MLCs were more likely to localize on blood vessels in DM without DR, NPDR, and PDR ($P < 0.05$ for all), but not healthy eyes.

CONCLUSIONS. MLC density was significantly increased in PDR. MLCs clustered on blood vessels in diabetic but not in healthy eyes. Further studies are needed to confirm the origin, identity, and function of MLCs during DR.

Keywords: optical coherence tomography angiography, OCT, OCTA, macula, retina, diabetic retinopathy, proliferative diabetic retinopathy

Advances in imaging and cell markers have greatly improved our understanding of the cell types present in the vitreous and retina. Optical coherence tomography (OCT) technology provides a detailed structural analysis of the retina and has become a mainstay for guiding treatment of retinal diseases. Recently, two key studies have used OCT to image macrophage-like cells (MLCs) located at the vitreoretinal interface.[1,2] These investigations visualized a 3- to 10-μm OCT slab above the vitreoretinal interface using either a clinical OCT angiography (OCTA) device[1] or adaptive optics OCT.[2] Both groups demonstrated that MLCs have a ramified morphology and are mobile, typical characteristics of macrophages.

Multiple populations of macrophage-related cells have been described in the retina that may contribute to vitreoretinal interface MLCs. Hyalocytes were first described in the 1840s and are considered resident macrophages of the cortical vitreous based on traditional macrophage marker expression.[3,4] After irradiation, hyalocytes are replenished by bone marrow–derived cells, supporting a macrophage lineage.[5] Furthermore, after retinal damage, hyalocytes can change their morphology, density, and cell signaling, which is also

a property of macrophages.[6,7] Retinal microglia are neural tissue-resident macrophages originating from the primitive yolk sac erythromyeloid progenitor that regulate the innate immune responses of the retina.[8,9] Microglia primarily reside in the inner and outer plexiform layers of the adult retina,[10] but an additional population can be visualized in the retinal nerve fiber layer (RNFL) and at the internal limiting membrane. Additionally, a perivascular macrophage population has been identified in the inner layers of the retina that lacks ionized calcium-binding adapter molecule 1, and expresses both F4/80 and macrophage scavenger receptor 1, features that distinguish perivascular macrophages from microglia.[11,12] Finally, monocyte-derived macrophages can infiltrate the retina, including the vitreoretinal interface, after blood–retinal barrier breakdown during experimental ischemia and vein occlusion in murine studies.[9,13] Therefore, potential identities of MLCs at the vitreoretinal interface include hyalocytes, microglia, perivascular macrophages, monocyte-derived macrophages, or a distinct cell type altogether.

In addition to MLC dendritiform morphology and migration, Castanos et al.[1] qualitatively showed that MLCs

1

localize to large blood vessels and display increased density in two eyes with ischemia from either central retinal vein occlusion or proliferative diabetic retinopathy (PDR). Based on these observations, we postulated that diabetic retinopathy (DR) pathology, which is characterized by retinal ischemia, blood–retinal barrier breakdown, and upregulation of cytokines,[14–16] may lead to activation, proliferation, or influx of MLCs from the circulation.[17,18] Regardless of their specific identity, it is unknown whether MLCs seen in OCT at the vitreoretinal interface play a role in the pathogenesis of DR. Contrary to Castanos et al.,[1] who described a lack of MLCs in the macula, we found that MLCs could be reliably identified in the macula. We hypothesized that macular MLC density would increase with DR severity and that MLCs would preferentially cluster on or near blood vessels. We performed OCTA imaging on healthy patients, patients with diabetes mellitus (DM) without DR, nonproliferative DR (NPDR), and PDR. We quantitatively assessed the density of MLCs and their relationship to underlying blood vessels in the superficial capillary plexus (SCP) using a semiautomated MLC thresholding technique. Overall, we found a significant increase in MLC density in PDR compared to all other groups, with the most substantial increase occurring in the perivascular space. We discuss the potential role of MLCs as inflammatory cells during proliferative disease and their relationship to the superficial vasculature.

MATERIALS AND METHODS

This prospective, cross-sectional study enrolled healthy subjects and patients with diabetes seen between October 2019 and December 2020 in the Department of Ophthalmology at Northwestern University in Chicago, Illinois. The study was approved by the Institutional Review Board of Northwestern University (IRB no. STU00200890) and conducted in accordance with the tenets of the Declaration of Helsinki and regulations of the Health Insurance Portability and Accountability Act. Written informed consent was obtained from all subjects before participation.

Inclusion criteria were age between 20 and 75 years old and, if applicable, diagnosis of DM without DR, NPDR, or PDR by a board-certified retina specialist. Patients were excluded if they had any other retinal disease such as age-related macular degeneration, anterior-segment disease including glaucoma, or significant media or lens opacities that could obscure images. Staging of DM without DR and NPDR eyes was performed by two independent graders (JXO and PLN) according to the International Clinical Diabetic Retinopathy Disease Severity Scale, by evaluating color fundus photographs obtained using the Ultra-Widefield Scanning Laser Ophthalmoscope (Optomap Panoramic 200; Optos PLC, Dunfermline, Scotland, UK) within 3 months of OCTA imaging.[19] Presence of central macular edema, defined as central macular thickness greater than 320 μm for men and 305 μm for women on Spectralis OCT (Heidelberg Engineering, Heidelberg, Germany) was also noted.[20]

OCTA Imaging

We used the RTVue-XR Avanti system (Optovue, Fremont, CA, USA) with split-spectrum amplitude-decorrelation angiography (SSADA) software (version 2017.1.0.151) to obtain repeat spectral domain–OCTA images over a nomi-

nal scan area of 3 × 3 mm (304 × 304 pixels) centered on the fovea.[21] The specifics of the device have been described previously.[22] We obtained repeated images (mean, 6.5 repeats; range, 3–10) of the same location in the retina. Only images with a Q score of 5 or greater and with limited motion artifact were included. For individuals with available imaging for both eyes, the eye with the highest average Q score was included.

We then segmented the full retinal vascular network OCTA slab from the inner limiting membrane (ILM) to 9 μm below the outer plexiform layer to use for registration between images. We segmented the MLC layer at the vitreoretinal interface using a 3-μm OCT slab located from 0 to 3 μm above the ILM (Figs. 1A, 1B). We segmented the RNFL using an OCT slab located from 0 to 27 μm below the ILM as previously described.[1] We segmented the SCP OCTA slab from the ILM to 10 μm above the inner plexiform layer. We exported these images into FIJI software,[23] a distribution of the program ImageJ (National Institutes of Health, Bethesda, MD, USA), and registered and averaged each layer as previously described.[1] In a subset of eyes, we followed the same procedure but obtained images centered on the edges of large areas of ischemia outside the macular region to analyze these lesions in the periphery.

Image Analysis

Binarization of Macrophage-Like Cells. MLCs were identified and isolated from the MLC layer OCT en face slab using a semiautomated binarization process implemented as a FIJI macro (see Supplementary File S1). This approach, which we developed based on methods for spot detection in fluorescence microscopy, included three general components—noise reduction to remove background irregularities and vessel artifacts, signal enhancement to improve cell identification, and binarization to extract discrete cell shapes.[24]

The image background was first flattened to correct for broad areas of uneven illumination and topologic variation at the foveal pit (Fig. 2B). A Gaussian blur of sigma 5.0 followed by inverse transformation was applied to the MLC layer OCT slab, after which the blurred and inverted image was added to the original image. A rolling ball background subtraction with radius 5 pixels was then applied to correct for smaller areas of background irregularity. Any remaining superficial vessel artifacts were manually removed, generating the "background-subtracted" image (Fig. 2C).

Signal enhancement and binarization were performed by a semiautomated seeding process to identify MLC locations on the background-subtracted image, followed by morphological dilation to probe and fill entire cell shapes. In generating the automated seeds, we sought to prioritize identification of high-intensity MLCs that could be distinguished from artifact with high certainty. The background-subtracted image was compensated to enhance the intensity of the MLCs while dimming bright artifacts introduced by the underlying RNFL layer. A Gaussian blur of sigma 2.0 followed by an inverse transformation was applied to the averaged RNFL OCT slab. This smaller sigma was chosen for the RNFL slab to preserve the contour of individual RNFL fibers. The blurred and inverted averaged RNFL OCT slab was averaged with the previously mentioned blurred and inverted MLC layer OCT slab and then multiplied by the background-subtracted image to generate a "compensated" image (Fig. 2D). Another rolling ball
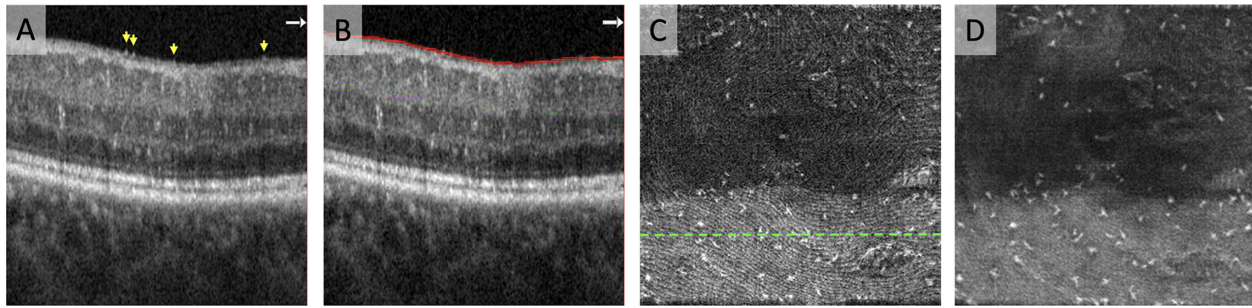
FIGURE 1. Segmentation, registration, and averaging of OCT slab containing MLCs. (**A**) OCT B-scan showing MLCs at the vitreoretinal interface. Profiles of individual MLCs are indicated by *yellow arrows* on the B-scan. (**B**) To isolate a layer containing MLCs, we segmented a 3-μm slab located directly above the internal limiting membrane. (**C**) Single scan of the 3-μm OCT en face slab containing MLCs. The *green dashed line* indicates the location of the B-scan shown in **A** and **B**. (**D**) Registered and averaged 3-μm OCT en face slab containing MLCs based on five repeated scans.
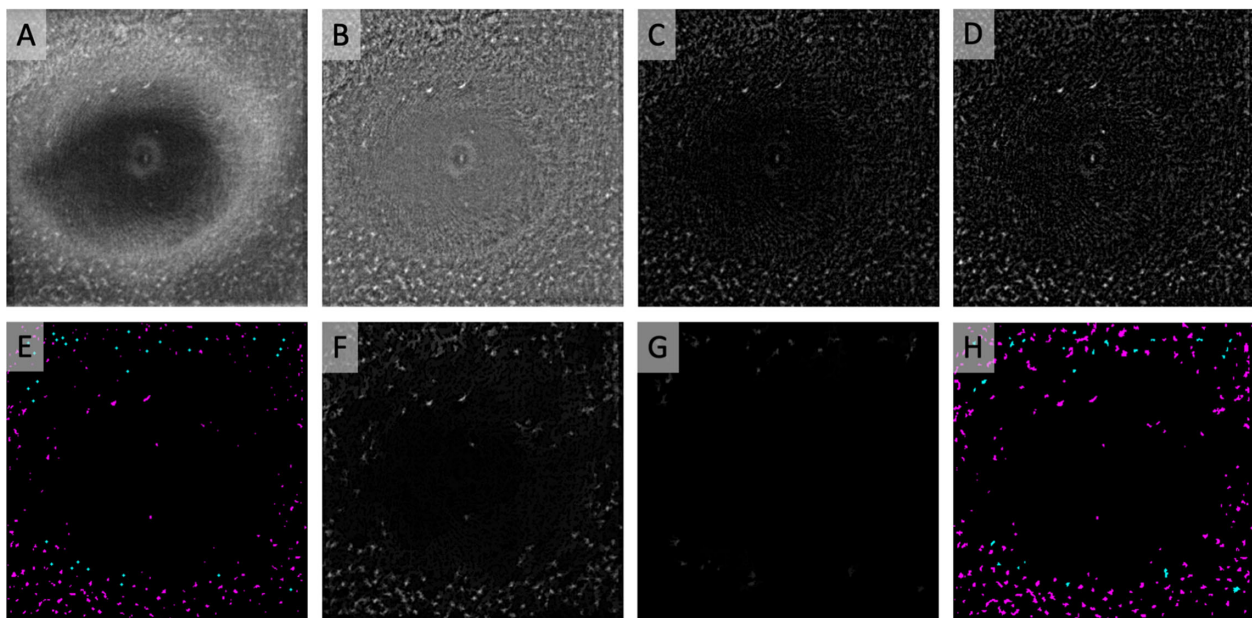
FIGURE 2. Semiautomated binarization protocol to identify MLCs. (**A**) Registered and averaged 3-μm OCT slab containing MLCs. (**B**) Background-flattened MLC layer OCT slab. (**C**) Background-subtracted slab from **B**. (**D**) MLC signal from **C** was compensated by multiplying against an averaged, inverted slab composed of the blurred MLC layer OCT and RNFL layer (not shown). (**E**) Automated (*magenta*) seeds were generated from the compensated image using MaxEntropy binarization. Manual seeds (*cyan; enlarged for clarity*) were placed on cells that were not identified by automated binarization. (**F**) Cells filled in by morphological dilation from automated seeds in **E**. (**G**) Manually seeded lower-intensity cells missed by automated seeding were filled in with a separate morphological dilation step. (**H**) Combined image containing binarized cells from automated seeding (*magenta*) and manual seeding (*cyan*).

background subtraction was applied, followed by binarization with MaxEntropy thresholding to generate a map of automatically identified macrophage seeds, which was corrected manually as necessary (Fig. 2E, magenta dots). This seed map provided a set of binarized markers for morphological dilation of the original background-subtracted image (Fig. 2F). Following dilation, the image was then binarized using global MaxEntropy thresholding.

Manual seeding was then performed as necessary to identify remaining MLCs. Single-pixel seeds were placed in the center of each missed cell (Fig. 2E, cyan dots). The manual seeds were used as markers for morphological dilation of the background-subtracted image (Fig. 2G), and the resulting image was binarized. Because MLCs identified by manual seeding were typically low-intensity cells missed

by the initial automated seeding, we binarized these cells using local Bernsen thresholding with a radius of 150 pixels instead of MaxEntropy thresholding, as this method qualitatively best preserved the outlines and sizes of the manually identified MLCs. The binarized images of automatically and manually identified cells were added together to generate a final image containing all binarized MLCs (Fig. 2H).

Müller Glial Cells. A small set of eyes ($n = 6$) was excluded from the analysis because these eyes demonstrated predominantly foveal hyperreflective foci consistent with retinal Müller glial cell foot plates at the ILM (Figs. 3A–3F).[25,26] These foci were significantly more likely to be located in the foveal avascular zone ($P < 0.05$). If Müller processes were present in eyes included in the study, we did not distinguish them from MLCs or remove them from
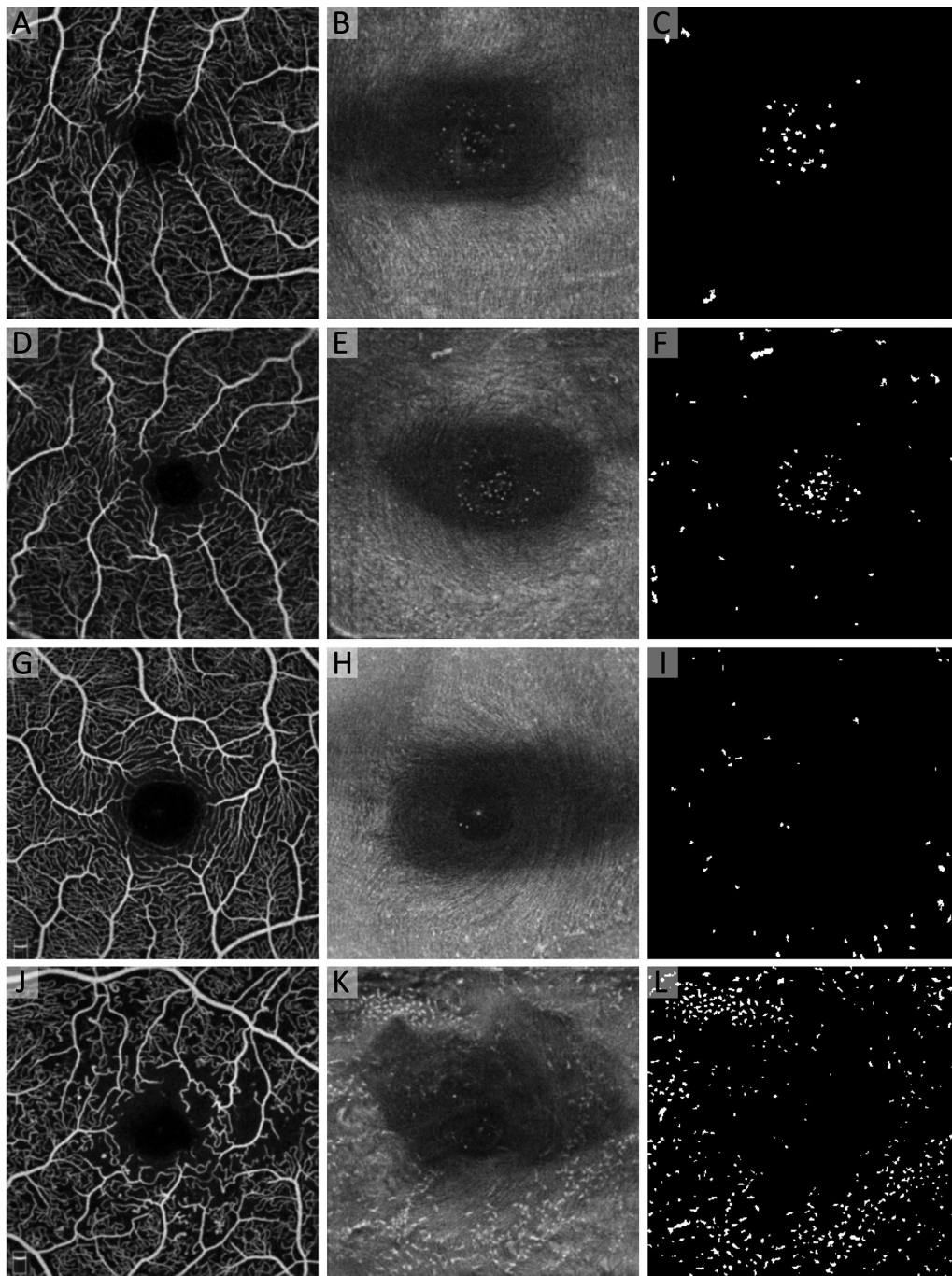
FIGURE 3. Eyes with predominately hyperreflective foci in the fovea consistent with retinal Müller glial cells were excluded. Eyes in the top two rows (**A–F**) were excluded from the analysis, whereas eyes in the bottom two rows (**G–L**) were included. The first column shows the aligned and averaged OCTA of the superficial capillary plexus. The middle column shows the aligned and averaged 3-µm OCT slab located from 0 to 3 µm above the ILM with (**B** and **E**) and without (**H** and **K**) clusters of hyperreflective dots in the foveal pit representing Müller glial foot plates. The third column shows the binarized map of the OCT showing the hyperreflective regions represented by white areas. Eyes with predominant Müller cell phenotype were excluded from the analysis (**A–F**).

the analysis, as they likely represented only a minimal percentage, if any, of the total cells identified in these scans (Figs. 3G–3L).

Characterization of MLC Parameters and Topographic Relation to Vessels. The number of MLCs was quantified from the binarized images using the Analyze Particles function. MLC density was calculated as the number

of cells over total image area (cells/mm^2). Vessel density was determined as the percentage of area occupied by blood vessels on the SCP OCTA slab following binarization with Huang thresholding. To test whether MLCs localized to different vascular compartments (vessels, perivascular, zones of ischemia), we first calculated the percentage of the total MLCs within each scan that directly overlapped with SCP

TABLE 1. Demographic Characteristics of Patients With MLCs

	Groups				
	Healthy	**DM Without DR**	**NPDR**	**PDR**	***P***
Subjects, *n*	18	22	17	15	—
Age (y), mean ± SD	38.7 ± 11.2	49.3 ± 14.3	45.5 ± 13.1	50.4 ± 13.1	0.040[*]
Sex (female), *n* (%)	10 (56)	13 (59)	10 (59)	5 (33)	0.409
Refractive error (D), mean ± SD	−1.32 ± 2.21	−2.93 ± 2.65	−2.15 ± 1.88	−0.56 ± 1.74	0.024[*,†]
Missing, *n* (%)	1 (5)	3 (14)	5 (29)	2 (13)	
Intraocular length, mean ± SD	24.10 ± 1.41	24.29 ± 1.04	24.21 ± 1.24	23.83 ± 1.28	0.885[†]
Missing, *n* (%)	11 (61)	9 (41)	9 (53)	9 (60)	—
DM type (type 1), *n* (%)	—	10 (45)	13 (76)	6 (40)	0.075
DM duration (y), mean ± SD	—	13.9 ± 11.2	23.2 ± 11.0	20.4 ± 10.4	0.030[*,†]
HbA1c, mean ± SD	—	6.8 ± 0.9	7.1 ± 0.7	7.6 ± 1.4	0.063[†]

All statistical tests for *P* values were nonparametric Kruskal–Wallis, unless indicated otherwise. Age showed a significant difference among groups (*P* < 0.05) but was not significantly different in any pairwise comparisons (all *P* > 0.05). Refractive error in DM without DR was significantly lower than in PDR (*P* < 0.05). DM duration was longer in NPDR compared with DM without DR (*P* < 0.05). HbA1c, hemoglobin A1c.
[*] Statistically significant (*P* < 0.05).
[†] Parametric one-way ANOVA.

TABLE 2. MLCs and Vascular Parameters in Healthy Controls and Different Diabetic Retinopathy Severity Groups

	Groups, Mean ± SD				
	Healthy	**DM Without DR**	**NPDR**	**PDR**	***P***
MLC count	52 ± 60	63 ± 55	48 ± 35	183 ± 157	<0.001[*]
MLC density (cells/mm^2)	6.4 ± 7.0	7.8 ± 6.5	5.8 ± 4.1	21.9 ± 19.4	<0.001[*]
Vessel density (%)	51.1 ± 3.5	49.5 ± 3.9	43.6 ± 4.5	37.5 ± 6.0	<0.001[*,†]
MLC density overlapping blood vessels (cells/mm^2)	7.0 ± 8.3	9.0 ± 8.0	6.8 ± 4.9	27.1 ± 22.8	<0.001[*]
Perivascular MLC density (cells/mm^2)	5.6 ± 6.2	7.1 ± 6.1	5.7 ± 4.5	23.7 ± 21.0	<0.001[*]
Ischemic MLC density (cells/mm^2)	5.5 ± 5.7	5.2 ± 4.0	3.8 ± 3.9	12.8 ± 13.1	0.002[*]
Distance to nearest blood vessel (μm)	12 ± 8	11 ± 9	15 ± 14	16 ± 7	0.098

All statistical tests for *P* values were nonparametric Kruskal–Wallis, unless indicated otherwise. When the overall test was significant, pairwise post hoc comparisons revealed that PDR significantly differed from each of the other three groups, including healthy control, DM without DR, and NPDR. The other three groups showed no significant differences from each other. Post hoc pairwise comparisons showed that PDR was the only group significantly different from the others, except for vessel density, which was significant for all pairwise comparisons (all *P* < 0.05), with the exception of healthy compared with DM without DR (*P* > 0.05).
[*] Statistically significant (*P* < 0.05).
[†] Parametric one-way ANOVA.

vessels. We then determined the percentage of MLCs located on the perivascular area within the 30-μm (3-pixel) watershed region surrounding SCP vessels, based on the predicted diffusion distance of an oxygen molecule from the center of a given blood vessel.[27] Finally, we measured the percentage of MLCs located in the ischemic area, which was defined as greater than 3 pixels (30 μm) from the nearest vessel. A strictly random MLC distribution would be expected to, on average, mirror the percentages of total area occupied by the corresponding vascular compartments. We adjusted the percentage of total MLCs within each vascular compartment by the percentage of total area occupied by each of these compartments and compared the resulting likelihoods to the random chance value of 1. We accounted for MLCs lying on the border between two different regions by counting them as partial cells within each region. We also calculated the MLC densities in these locations to obtain the number of MLCs per mm^2 of vessel area, perivascular area, and ischemic area.

A custom macro was implemented in FIJI to determine the average distance of MLCs to the nearest blood vessel. The binarized SCP image was iteratively enlarged to reflect increasing distance from the center of the SCP vessels, and the number of macrophages overlapping the enlarged SCP map at each distance value was quantified using the Analyze Particles function. The distance to the nearest blood vessel was calculated as a weighted average based on the fraction of macrophages at each distance.

Intra- and Inter-Rater Reliability of MLC Binarization. To assess the reliability of the semiautomated MLC binarization method, a random subset of 10 eyes was chosen for intra- and intergrader variability. MLC densities were determined two separate times by the same grader (JXO) masked to the results of their previous binarization to evaluate intra-rater reliability. Additionally, two masked graders (JXO and PLN) separately evaluated MLC densities to assess inter-rater reliability. The intragrader intraclass correlation coefficient (ICC) was 0.998 (95% confidence interval [CI], 0.993–1.000; *P* < 0.05) (Supplementary Fig. S1A), and the intergrader ICC was 0.995 (95% CI, 0.982–0.999; *P* < 0.05) (Supplementary Fig. S1B), demonstrating excellent rigor and reproducibility of our MLC binarization method.
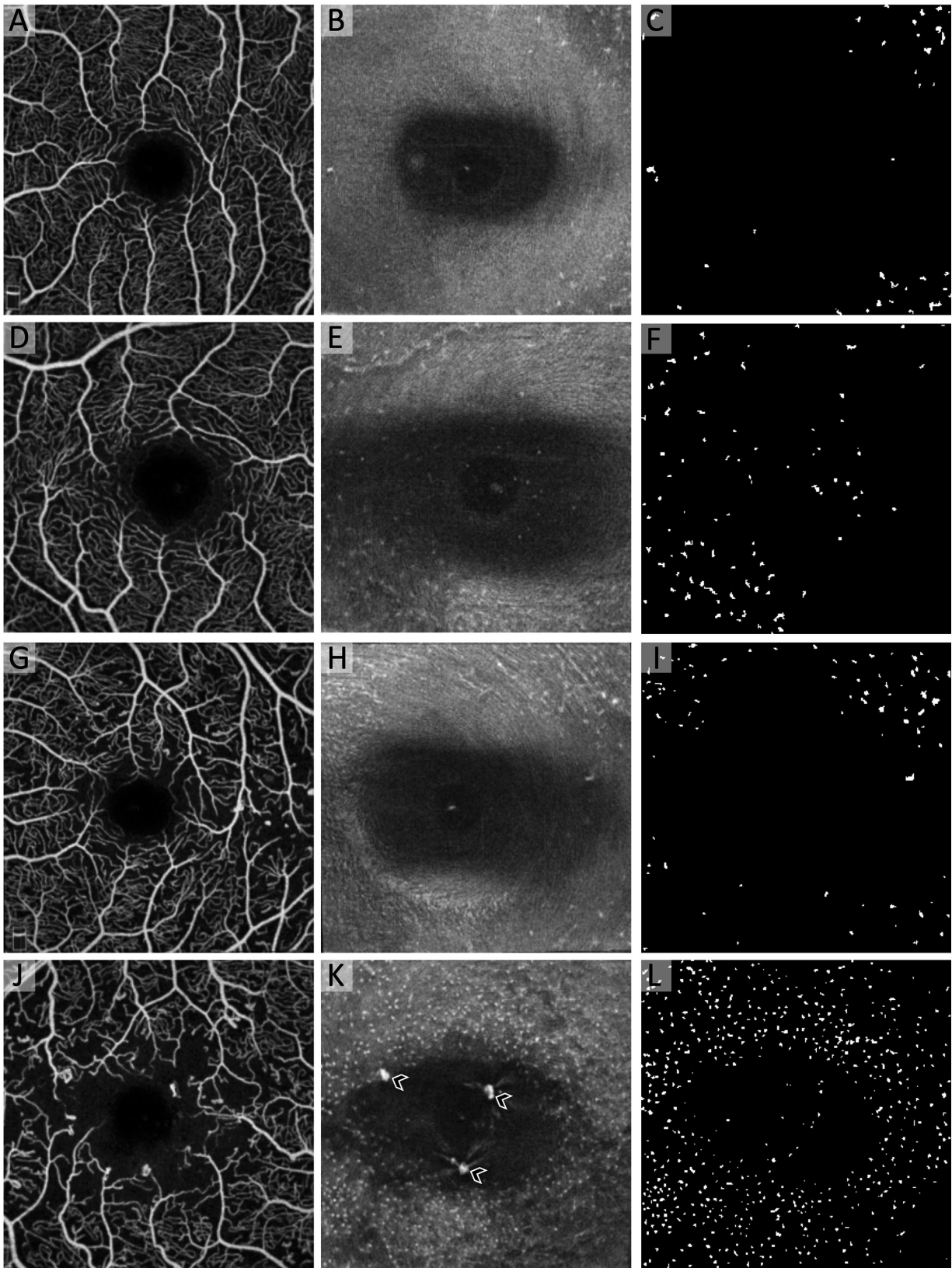
FIGURE 4. MLCs in healthy controls and increasing DR severity. From *top* to *bottom*, each row is a representative example of an eye from healthy control (**A–C**), DM without DR (**D–F**), NPDR (**G–I**), and PDR (**J–L**) groups. The first column shows the aligned and averaged OCTA of the superficial capillary plexus. The middle column shows the aligned and averaged 3-μm OCT slab located from 0 to 3 μm above the ILM with *hyperreflective dots* representing MLCs. The third column shows the binarized map of the OCT slab with MLCs shown in *white*. Note the large increase in cell density in the PDR group (**J–L**), with *arrowheads* highlighting pre-retinal neovascularization (**K**). There does not appear to be a spatial relationship between MLC and neovascularization in this eye.
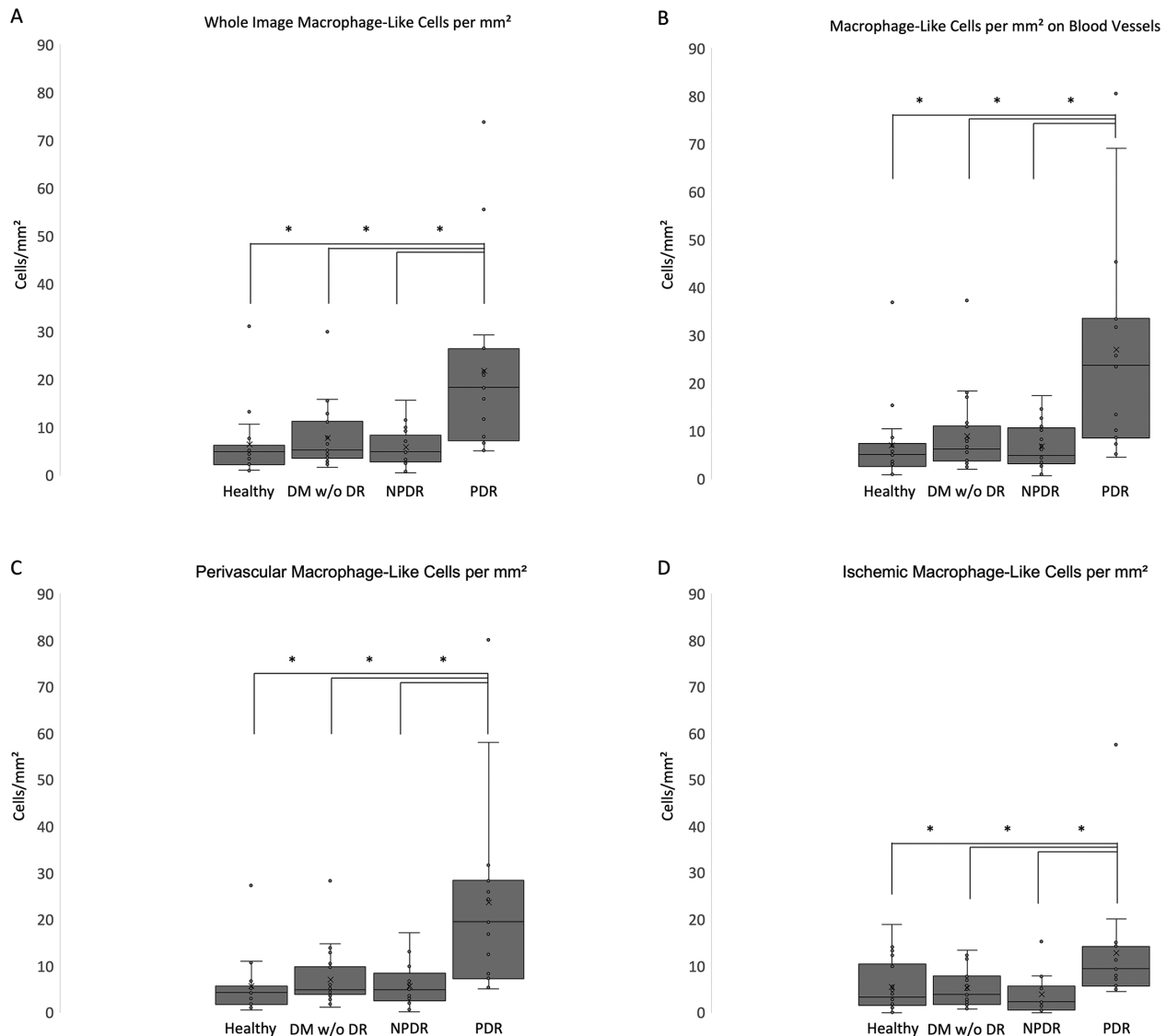
FIGURE 5. MLC density was significantly increased in PDR, most prominently in the perivascular region. Box-and-whisker plots with asterisks indicating statistically significant ($P < 0.05$) differences show an increase in MLC density in PDR compared with healthy controls, DM without DR), and NPDR. No other comparisons among groups were significant for MLC density.

Statistics

We used SPSS Statistics 27 (IBM Corp., Armonk, NY, USA) to perform statistical tests. For outcome variables, Shapiro–Wilk tests were significant for all but vessel density, as well as the percentage and likelihood of MLC overlapping with vascular and perivascular areas, indicating that much of the data deviated from a normal distribution. Levene's tests for equality of variances were not statistically significant, indicating that the data were homoscedastic. To compare MLC parameters between groups, we performed independent Kruskal–Wallis tests with post hoc Bonferroni correction for nonparametric data. We performed one-way analysis of variance (ANOVA) with Bonferroni correction for parametric data. We used one-sample t-tests with Bonferroni correction for multiple comparisons to evaluate the measured likelihoods of MLCs to be found in vascular, perivascular, and ischemic areas compared with random chance. Nonparametric Spearman rank correlations were used to explore the relationships among MLC parameters, vessel density, and demographic characteristics. Independent-sample t-tests were used when assessing the difference between only two groups based on demographics or treatment history. Absolute agreement ICCs were calculated for the reliability of intra- and inter-rater comparisons. $P < 0.05$ was considered statistically significant for all tests.

RESULTS

Seventy-two eyes of 72 subjects were included in the analysis (mean age, 46.0 ± 13.6 years; 38 females). Demographic characteristics for each group are shown in Table 1. Our sample consisted of healthy control eyes ($n = 18$), DM without DR eyes ($n = 22$), NPDR eyes ($n = 17$), and PDR eyes ($n = 15$). Intraocular length, sex, DM type (1 or 2), and hemoglobin A1c status were not significantly different among the groups, although there were minor differences
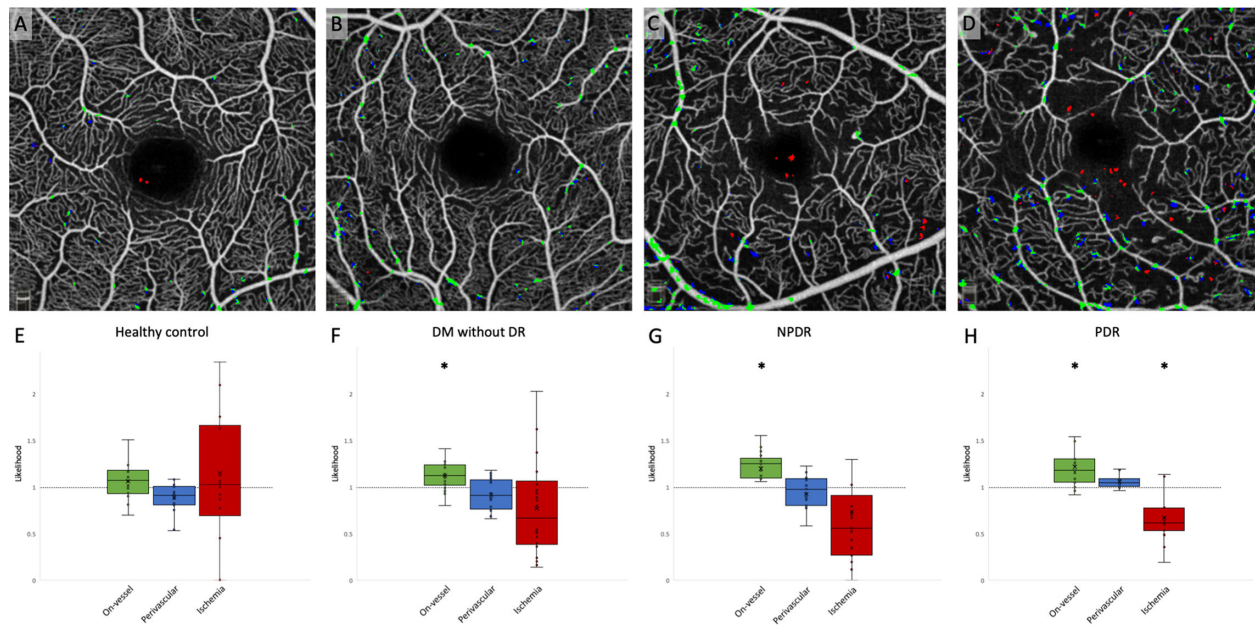
FIGURE 6. MLCs clustered on blood vessels in diabetes. *Top row*: OCTA of the superficial capillary plexus (SCP) in (**A**) healthy control, (**B**) DM without DR, (**C**) NPDR, and (**D**) PDR. *Pseudo-colored* pixels represent MLCs. *Green* MLCs colocalized with SCP vessels, *blue* MLCs are located in the perivascular area within 3 pixels (30 µm) of the nearest vessel, and *red* MLCs are located in the ischemic area more than 30 µm from the nearest vessel. MLCs with overlap in two regions are partially colored accordingly. *Bottom row*: Box-and-whisker plots showing MLC distribution on vessels (*green*), in perivascular regions (*blue*), and within zones of ischemia (*red*) for (**E**) healthy control, (**F**) DM without DR, (**G**) NPDR, and (**H**) PDR groups. Asterisks indicate statistically significant difference ($P < 0.05$) in likelihood based on one-sample *t*-tests compared with random chance likelihood of 1 (*dashed line*). *P* values were Bonferroni corrected for multiple comparisons. In all DM groups, MLCs were more likely to cluster on SCP vessels ($P < 0.05$ for all groups).

in refractive error and duration of DM (Table 1). PDR eyes either were treatment naïve ($n = 7$) or had been treated with PRP ($n = 3$), PRP plus focal laser ($n = 2$), PRP plus anti-vascular endothelial growth factor (VEGF; $n = 2$), or all three ($n = 1$). None of the eyes included in the study had central macular edema.

The MLC parameters from each group are summarized in Table 2, and representative examples are shown in Figure 4. Total MLC count was significantly greater in PDR compared with healthy controls (3.5-fold), DM without DR (2.9-fold), and NPDR (3.8-fold) (Table 2). The overall MLC density (cells/mm²) was significantly greater in PDR compared with healthy controls (3.4-fold), DM without DR (2.8-fold), and NPDR (3.8-fold) (Table 2, Fig. 5A). With respect to vascular localization, the MLC density in PDR was most increased in perivascular areas (3.3- to 4.2-fold; $P < 0.05$ vs. all groups) (Fig. 5C) and on blood vessels (3.0- to 4.0-fold; $P < 0.05$ vs. all groups) (Fig. 5B); it was also higher, although to a lesser extent, in ischemic areas (2.3- to 3.4-fold; $P < 0.05$ vs. all groups) (Fig. 5D).

We also investigated whether axial length or refractive error were correlated with MLC density, as axial length is capable of affecting image scale,[28] and in our study refractive error in DM without DR (-2.93 ± 2.65 diopters [D]) was significantly lower than in PDR (-0.56 ± 1.74 D; $P = 0.025$), with no other significant comparisons (all $P > 0.05$). We found no significant correlation with either parameter (Supplementary Figs. S2A, S2B). Next, in the subgroup of patients with axial length measurements ($n = 34$), we corrected MLC density for image scale as previously described.[29] We found that uncorrected MLC density in this subgroup was increased 1.8- to 3.0-fold in PDR eyes versus healthy, DM without DR, and NPDR eyes (Supple-

mentary Fig. S2C). In corrected eyes, MLC density remained 2.0- to 3.1-fold elevated in PDR compared with other groups (Supplementary Fig. S2D).

We found that MLCs did not show any significant clustering with respect to vascular, perivascular, or ischemic areas in healthy eyes ($P > 0.05$ for all). However, MLCs were significantly more likely to be located on vessels in DM without DR eyes (likelihood, 1.1 ± 0.1; $P < 0.05$), NPDR eyes (likelihood, 1.2 ± 0.2; $P < 0.05$), and PDR eyes (likelihood, 1.2 ± 0.2; $P < 0.05$) (Fig. 6). Additionally, in PDR, MLCs were significantly less likely than chance to be located in ischemic areas (likelihood, 0.7 ± 0.3; $P < 0.05$). There were no other significant distribution preferences in the other groups with respect to perivascular or ischemic areas ($P > 0.05$ for all).

A subset of eyes with severe NPDR ($n = 1$) and PDR ($n = 2$) was imaged in the posterior pole but outside of the macula. These participants showed large areas of total capillary signal loss with MLCs clustering near blood vessels that border the ischemic area, but a low number of cells within the ischemic area itself (Fig. 7). These scans had an average MLC density of 30.1 cells/mm² overall, with an MLC density of 40.8 cells/mm² on blood vessels (likelihood, 1.4), 33.9 cells/mm² in the perivascular space (likelihood, 1.1), and 18.8 cells/mm² in ischemia (likelihood, 0.6). These preliminary findings suggest that MLCs follow a similar pattern of clustering on blood vessels in the periphery as they do in the macula.

DISCUSSION

In this study, we sought to characterize MLCs and their distribution with respect to the underlying vasculature across
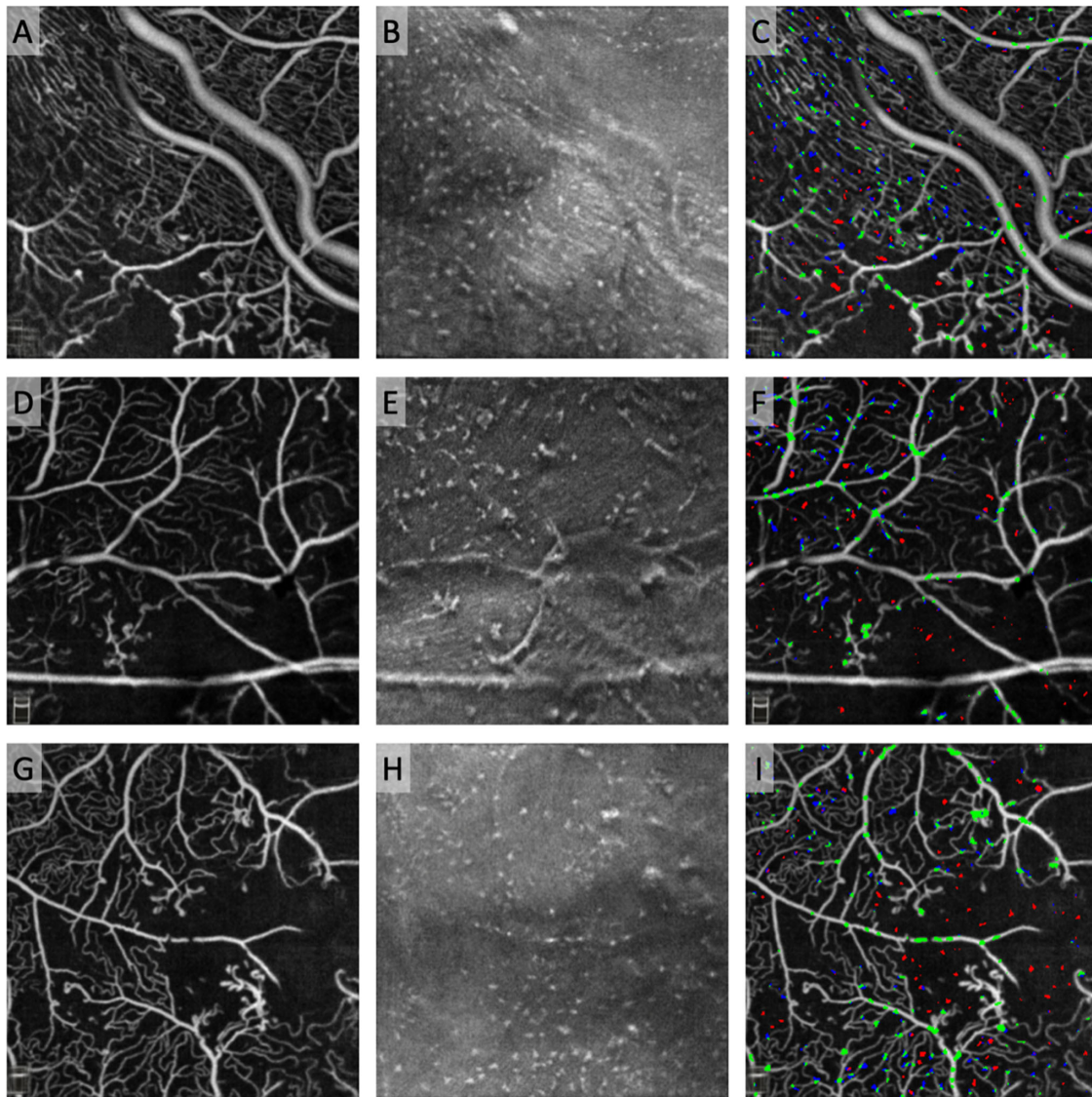
FIGURE 7. MLCs clustered around but not in large areas of ischemia outside the macula. *Top row*: Eye with severe NPDR imaged in the inferior quadrant near the vascular arcades. *Middle and bottom rows*: Eyes with PDR also imaged outside the macula. The first column shows the aligned and averaged OCTA of the SCP. The second column shows the aligned and averaged 3-μm OCT slab located from 0 to 3 μm above the ILM with *hyperreflective dots* representing MLCs. The third column shows the distribution of *pseudo-colored* MLCs overlaid on the OCTA image. *Green* MLCs colocalized with SCP vessels or to both blood vessels and the perivascular space, *blue* MLCs are located in the perivascular area within 3 pixels (~30 μm) of the nearest vessel, and *red* MLCs are located in the ischemic area more than ~30 μm from the nearest vessel or in both the ischemic area and perivascular space.

increasing DR severity. Overall, we found that total MLC density was significantly higher in PDR compared with healthy, DM without DR, and NPDR eyes (Fig. 5A). This increase was more pronounced in the perivascular region and on blood vessels than in ischemic areas (Figs. 5B–5D). Additionally, MLCs in all diabetic groups, but not in healthy eyes, were more likely than chance to cluster on blood vessels (Fig. 6). A sub-analysis of MLCs in large areas of ischemia outside the macula showed similarly high MLC densities and clustering on blood vessels, with sparse cells found within ischemic areas (Fig. 7).

Our results are consistent with the qualitative observations by Castanos et al.,[1] as well as with previous human histologic studies of MLC distribution in DR.[30] In human donor eyes, cells expressing human leukocyte antigen (HLA)-DR and CD68, markers associated with macrophages and activated microglia, are increased in NPDR and PDR compared with healthy controls.[30] These macrophages are observed anywhere in the retina from the ILM to the middle limiting membrane. Furthermore, these cells are identified in a perivascular distribution near areas with microaneurysms, hemorrhages, and/or neovascularization.[30] Thus, there is significant overlap between our findings and human histological investigations of macrophages. In addition, animal models of diabetes and chronic hyperglycemia have shown increased numbers of innate immune cells in the retina, although these studies did not use markers that could reliably discriminate between macrophages and microglia.[31–34]

Previous studies have identified innate immune cell activation and/or influx during NPDR.[30–34] However, we found no significant differences in MLC density in NPDR eyes,

only in PDR. Notably, 15 of the 17 NPDR eyes in our study had mild NPDR, whereas the remaining two had moderate NPDR. Additionally, the single severe NPDR eye that we imaged outside of the macula (Figs. 7A–7C) demonstrated MLC density similar to that of macular PDR eyes (Fig. 5) and extramacular PDR eyes (Figs. 7D–7I). The increasing ischemic burden in severe NPDR and PDR causes a shift to an actively proinflammatory and proangiogenic environment mediated by VEGF, cytokines, and chemokines that may contribute to the substantial increase in MLC density we observed.[16,35–37] Intravitreal injections of steroids, which have potent antiinflammatory properties, are used clinically to treat macular edema and are capable of regressing diabetic retinopathy.[38,39] Future investigations into quantitative MLC density during severe NDPR, macular edema, and after intravitreal steroid therapy may uncover new associations and the potential role of MLCs in DR pathology.

In addition to MLC density, we also investigated MLC distribution relative to the location of blood vessels and ischemia. We showed that in all diabetic groups, but not in healthy eyes, MLCs were more likely than chance to be found on blood vessels, and furthermore in PDR were less likely than chance to be found in ischemic areas (Fig. 6). We observed similar MLC localization preferences for blood vessels in images outside the macula. There are several possible reasons for this finding. First, DR causes endothelial damage and pericyte loss, leading to dysfunction of the blood–retinal barrier; thus, these MLCs could be monocyte-derived macrophages from the leaky vasculature.[40] Second, the localization of MLCs to blood vessels could reflect their potential origin as perivascular macrophages, which may expand for reparative functions to maintain the diseased vasculature. Third, MLCs may be reliant upon oxidative phosphorylation and thus prefer to avoid the ischemic regions; because pro-angiogenic macrophages primarily rely upon glycolysis,[41] this hypothesis would suggest a restorative rather than pathologic role of MLCs in DR. Future studies in animal models will be necessary to definitively determine the origin and function of MLCs.

Microglial activation is characterized by a change in their shapes from stellate to amoeboid cells, and hyalocyte activation is similarly associated with morphologic change.[16,34,42] Although we were able to binarize MLC outlines, we were unable to reliably quantify changes in MLC morphology using metrics such as size and circularity due to the limited resolution of the OCTA device. Our preliminary attempts to quantify MLC size using this dataset suggested an average area on the order of 1000 µm² per cell, corresponding to an approximate MLC length of 32 µm, which the reported 15-µm resolution of the Optovue OCTA would be insufficient to accurately quantify. Investigation using a higher resolution imaging modality such as adaptive optics OCT would be necessary for further characterization of MLC morphologic changes in diabetic eye disease.

There are several limitations to our study, including the sample size, which was restricted by the requirements of the imaging protocol, and the large fraction of previously treated patients (8/15) in the PDR group. Although we found no significant differences in MLC parameters between treatment-naïve and treated eyes (both groups had increased MLC density), anti-VEGF injection or laser treatment could potentially alter MLC activity or proliferation. Studies on how treatment affects MLC density would be important areas of future investigation. Additionally, individual variations in refractive error and axial length would affect the image

scale, effectively increasing (longer axial length) or decreasing (shorter axial length) the field of view for MLCs imaged in a given eye, an effect that must be considered in MLC density quantifications.[43] In the subgroup of patients with axial length measurements, corrected MLC density in PDR patients remained elevated compared to healthy, DM without DR, and NPDR eyes (Supplementary Fig. S2). Furthermore, in the subgroup of patients with known refractive error, PDR eyes were the least myopic (Table 1), making the field of view in PDR eyes the smallest on average compared to the other groups. It would be expected that, because of the smaller field of view, the number of MLCs counted in our study would overall be artificially lowered in the PDR group; therefore, we do not believe that scaling affected our overall findings.

In conclusion, we found that macular MLC density is significantly higher in PDR, with the largest proportional increase occurring on and near blood vessels. The origin, identity, and function of MLCs remain unknown. Because the vitreoretinal interface is a highly important anatomical location for PDR pathology, including neovascularization and membrane formation, this novel association may have important clinical relevance to PDR pathogenesis.

Disclosure: **J.X. Ong**, None; **P.L. Nesper**, None; **A.A. Fawzi**, None; **J.M. Wang**, None; **J.A. Lavine**, None

References

1. Castanos MV, Zhou DB, Linderman RE, et al. Imaging of macrophage-like cells in living human retina using clinical OCT. *Invest Ophthalmol Vis Sci*. 2020;61(6):48.

2. Hammer DX, Agrawal A, Villanueva R, Saeedi O, Liu Z. Label-free adaptive optics imaging of human retinal macrophage distribution and dynamics. *Proc Natl Acad Sci USA*. 2020;117(48):30661–30669.

3. Vagaja NN, Chinnery HR, Binz N, Kezic JM, Rakoczy EP, McMenamin PG. Changes in murine hyalocytes are valuable early indicators of ocular disease. *Invest Ophthalmol Vis Sci*. 2012;53(3):1445–1451.

4. Hamburg A. Some investigations on the cells of the vitreous body. *Ophthalmologica*. 1959;138(2):81–107.

5. Qiao H, Hisatomi T, Sonoda KH, et al. The characterisation of hyalocytes: the origin, phenotype, and turnover. *Br J Ophthalmol*. 2005;89(4):513–517.

6. Lazarus HS, Schoenfeld C-L, Fekrat S, et al. Hyalocytes synthesize and secrete inhibitors of retinal pigment epithelial cell proliferation in vitro. *Arch Ophthalmol*. 1996;114(6):731–736.

7. Gloor BP. Mitotic activity in the cortical vitreous cells (hyalocytes) after photocoagulation. *Invest Ophthalmol Vis Sci*. 1969;8(6):633–646.

8. Hefendehl JK, Neher JJ, Sühs RB, Kohsaka S, Skodras A, Jucker M. Homeostatic and injury-induced microglia

behavior in the aging brain. *Aging Cell*. 2014;13(1):60–69.

9. Zhang C, Lam TT, Tso MO. Heterogeneous populations of microglia/macrophages in the retina and their activation after retinal ischemia and reperfusion injury. *Exp Eye Res*. 2005;81(6):700–709.

10. O'Koren EG, Yu C, Klingeborn M, et al. Microglial function is distinct in different anatomical locations during retinal homeostasis and degeneration. *Immunity*. 2019;50(3):723–737.e7.

11. Mendes-Jorge L, Ramos D, Luppo M, et al. Scavenger function of resident autofluorescent perivascular macrophages and their contribution to the maintenance of the blood–retinal barrier. *Invest Ophthalmol Vis Sci*. 2009;50(12):5997–6005.

12. Roubeix C, Dominguez E, Raoul W, et al. Mo-derived perivascular macrophage recruitment protects against endothelial cell death in retinal vein occlusion. *J Neuroinflammation*. 2019;16(1):157.

13. Ebneter A, Kokona D, Schneider N, Zinkernagel MS. Microglia activation and recruitment of circulating macrophages during ischemic experimental branch retinal vein occlusion. *Invest Ophthalmol Vis Sci*. 2017;58(2):944–953.

14. Tang J, Kern TS. Inflammation in diabetic retinopathy. *Prog Retin Eye Res*. 2011;30(5):343–358.

15. Zhang W, Liu H, Al-Shabrawey M, Caldwell RW, Caldwell RB. Inflammation and diabetic retinal microvascular complications. *J Cardiovasc Dis Res*. 2011;2(2):96–103.

16. Altmann C, Schmidt MHH. The role of microglia in diabetic retinopathy: inflammation, microvasculature defects and neurodegeneration. *Int J Mol Sci*. 2018;19(1):110.

17. Witmer A, Vrensen G, Van Noorden C, Schlingemann R. Vascular endothelial growth factors and angiogenesis in eye disease. *Prog Retin Eye Res*. 2003;22(1):1–29.

18. Wang W, Lo AC. Diabetic retinopathy: pathophysiology and treatments. *Int J Mol Sci*. 2018;19(6):1816.

19. Wilkinson CP, Ferris FL, 3rd, Klein RE, et al. Proposed international clinical diabetic retinopathy and diabetic macular edema disease severity scales. *Ophthalmology*. 2003;110(9):1677–1682.

20. Diabetic Retinopathy Clinical Research Network,Elman MJ, Aiello LP, et al. Randomized trial evaluating ranibizumab plus prompt or deferred laser or triamcinolone plus prompt laser for diabetic macular edema. *Ophthalmology*. 2010;117(6):1064–1077.e35.

21. Jia Y, Tan O, Tokayer J, et al. Split-spectrum amplitude-decorrelation angiography with optical coherence tomography. *Opt Express*. 2012;20(4):4710–4725.

22. Nesper PL, Lee HE, Fayed AE, Schwartz GW, Yu F, Fawzi AA. Hemodynamic response of the three macular capillary plexuses in dark adaptation and flicker stimulation using optical coherence tomography angiography. *Invest Ophthalmol Vis Sci*. 2019;60(2):694–703.

23. Schindelin J, Arganda-Carreras I, Frise E, et al. Fiji: an open-source platform for biological-image analysis. *Nat Methods*. 2012;9(7):676–682.

24. Smal I, Loog M, Niessen W, Meijering E. Quantitative comparison of spot detection methods in fluorescence microscopy. *IEEE Trans Med Imaging*. 2010;29(2):282–301.

25. Tschulakow AV, Oltrup T, Bende T, Schmelzle S, Schraermeyer U. The anatomy of the foveola reinvestigated. *PeerJ*. 2018;6:e4482.

26. Delaunay K, Khamsy L, Kowalczuk L, et al. Glial cells of the human fovea. *Mol Vis*. 2020;26:235–245.

27. Chen S, Moult EM, Zangwill LM, Weinreb RN, Fujimoto JG. Geometric perfusion deficits: a novel OCT angiography biomarker for diabetic retinopathy based on oxygen diffusion. *Am J Ophthalmol*. 2020;222:256–270.

28. Llanas S, Linderman RE, Chen FK, Carroll J. Assessing the use of incorrectly scaled optical coherence tomography angiography images in peer-reviewed studies: a systematic review. *JAMA Ophthalmol*. 2020;138(1):86–94.

29. Linderman R, Salmon AE, Strampe M, Russillo M, Khan J, Carroll J. Assessing the accuracy of foveal avascular zone measurements using optical coherence tomography angiography: segmentation and scaling. *Transl Vis Sci Technol*. 2017;6(3):16.

30. Zeng HY, Green WR, Tso MO. Microglial activation in human diabetic retinopathy. *Arch Ophthalmol*. 2008;126(2):227–232.

31. Omri S, Behar-Cohen F, de Kozak Y, et al. Microglia/macrophages migrate through retinal epithelium barrier by a transcellular route in diabetic retinopathy: role of PKCζ in the Goto Kakizaki rat model. *Am J Pathol*. 2011;179(2):942–953.

32. Gaucher D, Chiappore JA, Paques M, et al. Microglial changes occur without neural cell death in diabetic retinopathy. *Vision Res*. 2007;47(5):612–623.

33. Zeng XX, Ng YK, Ling EA. Neuronal and microglial response in the retina of streptozotocin-induced diabetic rats. *Vis Neurosci*. 2000;17(3):463–471.

34. Krady JK, Basu A, Allen CM, et al. Minocycline reduces proinflammatory cytokine expression, microglial activation, and caspase-3 activation in a rodent model of diabetic retinopathy. *Diabetes*. 2005;54(5):1559–1565.

35. Adamis AP, Miller JW, Bernal MT, et al. Increased vascular endothelial growth factor levels in the vitreous of eyes with proliferative diabetic retinopathy. *Am J Ophthalmol*. 1994;118(4):445–450.

36. Scott IU, Jackson GR, Quillen DA, Klein R, Liao J, Gardner TW. Effect of doxycycline vs placebo on retinal function and diabetic retinopathy progression in mild to moderate nonproliferative diabetic retinopathy: a randomized proof-of-concept clinical trial. *JAMA Ophthalmol*. 2014;132(9):1137–1142.

37. Scott IU, Jackson GR, Quillen DA, et al. Effect of doxycycline vs placebo on retinal function and diabetic retinopathy progression in patients with severe nonproliferative or non-high-risk proliferative diabetic retinopathy: a randomized clinical trial. *JAMA Ophthalmol*. 2014;132(5):535–543.

38. Gillies MC, Simpson JM, Gaston C, et al. Five-year results of a randomized trial with open-label extension of triamcinolone acetonide for refractory diabetic macular edema. *Ophthalmology*. 2009;116(11):2182–2187.

39. Bandello F, Preziosa C, Querques G, Lattanzio R. Update of intravitreal steroids for the treatment of diabetic macular edema. *Ophthalmic Res*. 2014;52(2):89–96.

40. Hammes HP, Feng Y, Pfister F, Brownlee M. Diabetic retinopathy: targeting vasoregression. *Diabetes*. 2011;60(1):9–16.

41. Liu Z, Xu J, Ma Q, et al. Glycolysis links reciprocal activation of myeloid cells and endothelial cells in the retinal angiogenic niche. *Sci Transl Med*. 2020;12(555):eaay1371.

42. Sakamoto T, Ishibashi T. Hyalocytes: essential cells of the vitreous cavity in vitreoretinal pathophysiology? *Retina*. 2011;31(2):222–228.

43. Wen C, Pei C, Xu X, Lei J. Influence of axial length on parafoveal and peripapillary metrics from swept source optical coherence tomography angiography. *Curr Eye Res*. 2019;44(9):980–986.